Monthly Notices
of the
ROYAL ASTRONOMICAL SOCIETY

MNRAS **475,** 4011–4019 (2018)
Advance Access publication 2018 January 10

doi:10.1093/mnras/sty077

Long-term radio and X-ray evolution of the tidal disruption event ASASSN-14li

J. S. Bright,[1★] R. P. Fender,[1★] S. E. Motta,[1] K. Mooley,[1] Y. C. Perrott,[2] S. van Velzen,[3] S. Carey,[2] J. Hickish,[2] N. Razavi-Ghods,[2] D. Titterington,[2] P. Scott,[2] K. Grainge,[4] A. Scaife,[4] T. Cantwell[4] and C. Rumsey[2]

[1]*Department of Physics, University of Oxford, Denys Wilkinson Building, Keble Road, Oxford OX1 3RH, UK*
[2]*Astrophysics Group, Cavendish Laboratory, 19 J. J. Thomson Avenue, Cambridge CB3 0HE, UK*
[3]*Department of Physics and Astronomy, The Johns Hopkins University, Baltimore, MD 21218, USA*
[4]*Jodrell Bank Centre for Astrophysics, Alan Turing Building, School of Physics and Astronomy, University of Manchester M13 9PL, UK*

Accepted 2017 December 27. Received 2017 December 7; in original form 2017 October 18

ABSTRACT

We report on late time radio and X-ray observations of the tidal disruption event candidate ASASSN-14li, covering the first 1000 d of the decay phase. For the first ∼200 d the radio and X-ray emission fade in concert. This phase is better fitted by an exponential decay at X-ray wavelengths, while the radio emission is well described by either an exponential or the canonical $t^{-5/3}$ decay assumed for tidal disruption events. The correlation between radio and X-ray emission during this period can be fitted as $L_{\rm R} \propto L_{\rm X}^{1.9\pm0.2}$. After 400 d the radio emission at 15.5 GHz has reached a plateau level of 244 ± 8 μJy which it maintains for at least the next 600 d, while the X-ray emission continues to fade exponentially. This steady level of radio emission is likely due to relic radio lobes from the weak AGN-like activity implied by historical radio observations. We note that while most existing models are based upon the evolution of ejecta which are decoupled from the central black hole, the radio–X-ray correlation during the declining phase is also consistent with core-jet emission coupled to a radiatively efficient accretion flow.

Key words: accretion, accretion discs – black hole physics – galaxies: jets – X-rays: individual: ASASSN-14li.

1 INTRODUCTION

A tidal disruption event (TDE) occurs when a stellar object passes close to a supermassive black hole (SMBH) on a highly eccentric orbit which is potentially misaligned with the black hole's spin, and is torn apart when strong tidal forces overcome the star's self-gravity. Approximately half of the mass of the disrupted object forms a complex accretion flow on to the SMBH, while the other half becomes unbound and is ejected from the system (see e.g. Rees 1988 and Guillochon, Manukian & Ramirez-Ruiz 2014). TDEs can be identified through their strong blue continuum, showing significant brightening in optical, UV – and sometimes X-ray – compared to archival observations of the host galaxy. Spectral signatures of TDEs include broad hydrogen (Balmers series) emission lines as well as emission in He I and He II, although the abundance of specific elements varies significantly between events (Arcavi et al. 2014). The critical radius for disruption, where tidal effects become dominant, is $R_{\rm p} \sim R_{\rm tidal} = R_\star (M_{\rm BH}/M_\star)^{1/3}$, where $R_{\rm p}$ is the pericentre distance of the star's orbit. The tidal radius must be outside the black hole's Schwarzschild radius in order for the flaring associated with these events to be observed.

TDE candidates are typically discovered through optical (e.g. van Velzen et al. 2011; Holoien et al. 2016), UV (e.g. Gezari et al. 2009), or X-ray emission (e.g. Komossa & Bade 1999; Esquej et al. 2007) from the initial accretion flow and resulting flare in transient surveys, and are confirmed as TDEs based on their decay characteristics and spectra. The accretion flow formed in a TDE is unlike classical AGN accretion discs, consisting of orders of magnitude less mass but producing significantly higher accretion rates, which can be (initially) super-Eddington. The material that remains bound to the SMBH is expected to form an accretion disc, with the circularization time-scale depending on relativistic precession effects, which dictate the chance of stream self-interaction (Hayasaki, Stone & Loeb 2013; Guillochon & Ramirez-Ruiz 2015; Bonnerot et al. 2016) and are in part dictated by the spin of the SMBH. It has also been shown (Hayasaki et al. 2013) that the radiative cooling efficiency can affect the circularization time-scale, as well as the thickness of the disc. The observational signatures of such an

★ E-mail: joe.bright@physics.ox.ac.uk (JSB); rob.fender@physics.ox.ac.uk (RPF)

accretion flow will depend on the circularization, radiative cooling, and viscous time-scales which are described and discussed by Evans & Kochanek (1989) and Bonnerot et al. (2016). Alternatively, it has been suggested (Piran et al. 2015; Pasham et al. 2017) that the dominant component of the optical/UV emission could be the result of the bound debris stream self-interacting (and shocking) as it circles the black hole, with the disc predominantly contributing X-ray emission.

ASASSN-14li was discovered by the All Sky Automated Search for Supernova (ASASSN; Shappee et al. 2014) on UT 2014–11–22.63 (MJD 56983.6) as a 16.5 magnitude source in the *V* band (Jose et al. 2014; Holoien et al. 2016; Brown et al. 2017a). The position of the source was found to be consistent with the centre of the post-starburst galaxy PGC 043234, with a measured projected separation of 0.04 arcsec. This galaxy is at redshift $z = 0.0206$ with a luminosity distance of 90.3 Mpc (for cosmological parameters $H_0 = 73\,\mathrm{kms}^{-1}\,\mathrm{Mpc}^{-1}$, $\Omega_{\mathrm{matter}} = 0.27$, and $\Omega_\Lambda = 0.73$). It was established through archival X-ray observations of PGC 043234 from the ROSAT All-Sky Survey (Voges et al. 1999) that the galaxy does not contain an efficiently accreting AGN, with the count rate implying a luminosity orders of magnitude below standard active nuclei (e.g. Miller et al. 2015). A small number (currently six) of confirmed TDEs, including ASASSN-14li, have also been detected at radio wavelengths and the population may form a bi-modal distribution, consisting of more common non-relativistic 'thermal' events and rarer relativistic jets. Three events (Swift J1644+57; Burrows et al. 2011; Zauderer et al. 2011, Swift J2058+05; Cenko et al. 2012, Swift J1112.2; Brown et al. 2017b) have isotropic ∼5 GHz luminosities of between 10^{40} and $10^{42}\,\mathrm{erg\,s}^{-1}$ whereas the rest (IGR J12580+0134; Irwin et al. 2015, XMMSL1 J0740-85; Alexander et al. 2017, ASASSN-14li; van Velzen et al. 2016; Alexander et al. 2016) have luminosities in the range 10^{37} to $10^{39}\,\mathrm{erg\,s}^{-1}$ at similar frequencies. The higher power events are believed to result from observing down the axis of a relativistic jet, resulting in the energy of photons being significantly boosted. Even accounting for boosting, these relativistic events have a higher total energy output than their thermal counterparts. The origin of the radio emission from the thermal events is currently uncertain, with transient jets (van Velzen et al. 2016), non-relativistic winds (Alexander et al. 2016), and shocks driven by unbound material (Krolik et al. 2016) all feasible scenarios. ASASSN-14li is by far the best studied of the 'thermal' TDE category, having been observed extensively at Optical, UV, X-ray (where ASASSN-14li is unusually loud for an optically selected TDE), and radio wavelengths. The high cadence X-ray and radio observations in particular allow for the X-ray/radio coupling to be probed.

We organize this paper as follows: in Section 2 we describe our radio and X-ray observations of ASASSN-14li and their analysis. In Sections 3 and 4 we show our correlation of the multi-wavelength data, and demonstrate that ASASSN-14li has now faded below its host galaxy's background radio emission. Our results are summarized in Section 5, with all radio and X-ray data used given in the Appendix.

2 OBSERVATIONS

2.1 *Swift* X-ray observations

Swift (Gehrels et al. 2004) observations of ASASSN-14li were first initiated on 56991.5 and a total of 102 observing segments have been conducted to date [100 of which had photon counting (PC) mode data], with exposure times ranging between 90 and 4000 s. The six segments between 57819.6 and 57833.5 were triggered due to a target of opportunity request submitted by the authors, whereas all other observations are archival. The position of the source was measured as J2000 RA/Dec. = $12^{\mathrm{h}}\,48^{\mathrm{m}}\,15\overset{\mathrm{s}}{.}05/+17^\circ\,46'\,31\overset{''}{.}5$ with a circular 90 per cent confidence region of radius 3.5 arcsec (Goad et al. 2007; Evans et al. 2009). The source was observed multiple times per week for the first ∼200 d post-flare, and more sporadically afterwards. Observations utilized the X-ray telescope (XRT) instrument in PC mode as well as the ultra violet and optical telescope (UVOT), with the exact filter depending on the observation. We are primarily interested in the X-ray data, and the *Swift* XRT product generator online reduction pipeline (Evans et al. 2007; Evans et al. 2009) was used to extract count rates in the 0.3–10 keV energy band from the observations. In order to probe the X-ray–radio luminosity correlation we converted our count rates into fluxes. To do this, we first binned the X-ray light curve of ASASSN-14li into six broad time bins and extracted a spectrum from each bin. We defined the bins in a way that allowed us to both obtain acceptable signal-to-noise ratio spectra and to evenly sample the decay phase of ASASSN-14li. These spectra were then fitted with an absorbed blackbody model, from which the flux could be calculated. We fitted the spectra with an absorbed[1] blackbody component. The resulting best fits show a blackbody temperature variation consistent with those reported by Miller et al. (2015). The relationship between flux and counts across the six bins was described by a linear fit, which was then used to convert the full light curve from count rate to flux. The *Swift* X-ray light curve is shown in the bottom panel of Fig. 1.

2.2 Arcminute Microkelvin Imager Large Array radio observations – light curve

Radio observations of ASASSN-14li were initiated with the Arcminute Microkelvin Imager Large Array (Zwart et al. 2008; Hickish et al. 2018), hereafter AMI-LA, on MJD 57014.1, about 22 d after the first *Swift* observations of the source. ASASSN-14li was monitored on an approximately weekly basis (apart from a significant gap between ∼180 and ∼400 d post-flare due to technical work being performed on the AMI-LA) with typical exposures lasting between 2 and 4 h, yielding an rms flux in a typical image of ∼35 and 25 μJy, respectively. Observations pre-MJD − 56983.6 = 200 were taken with an analogue correlator at an effective central frequency of 15.7 GHz, and are published in van Velzen et al. (2016). Observations after the gap utilized the new digital correlator, which has 4096 channels across a 5 GHz bandwidth between 13 and 18 GHz and are first published in this manuscript. J1255+1817 was used as the interleaved phase calibrator and was observed for ∼2 min for every ∼10 min on source while 3C286 and 3C48 were used for absolute flux calibration. The AMI-LA data were binned into eight channels, each of width 0.625 GHz, and were calibrated and flagged for radio frequency interference (RFI) using the automated AMI reduction software pipeline REDUCE (e.g. Davies et al. 2009). The data were then imported into CASA (McMullin et al. 2007) where additional RFI flagging was performed using the FLAGDATA task in RFLAG mode, which removed interference localized in time and frequency at the 3σ level. The data were then cleaned using the CLEAN task, with a stopping threshold of three times the background rms of the image and a gain of 0.1. To calculate flux measurements from ASASSN-14li we used the PYTHON-based PySE source extraction software, which was developed as part of the LOFAR Transient

[1] $N_{\mathrm{H}} = 1.6 \times 10^{20}\mathrm{cm}^2$.

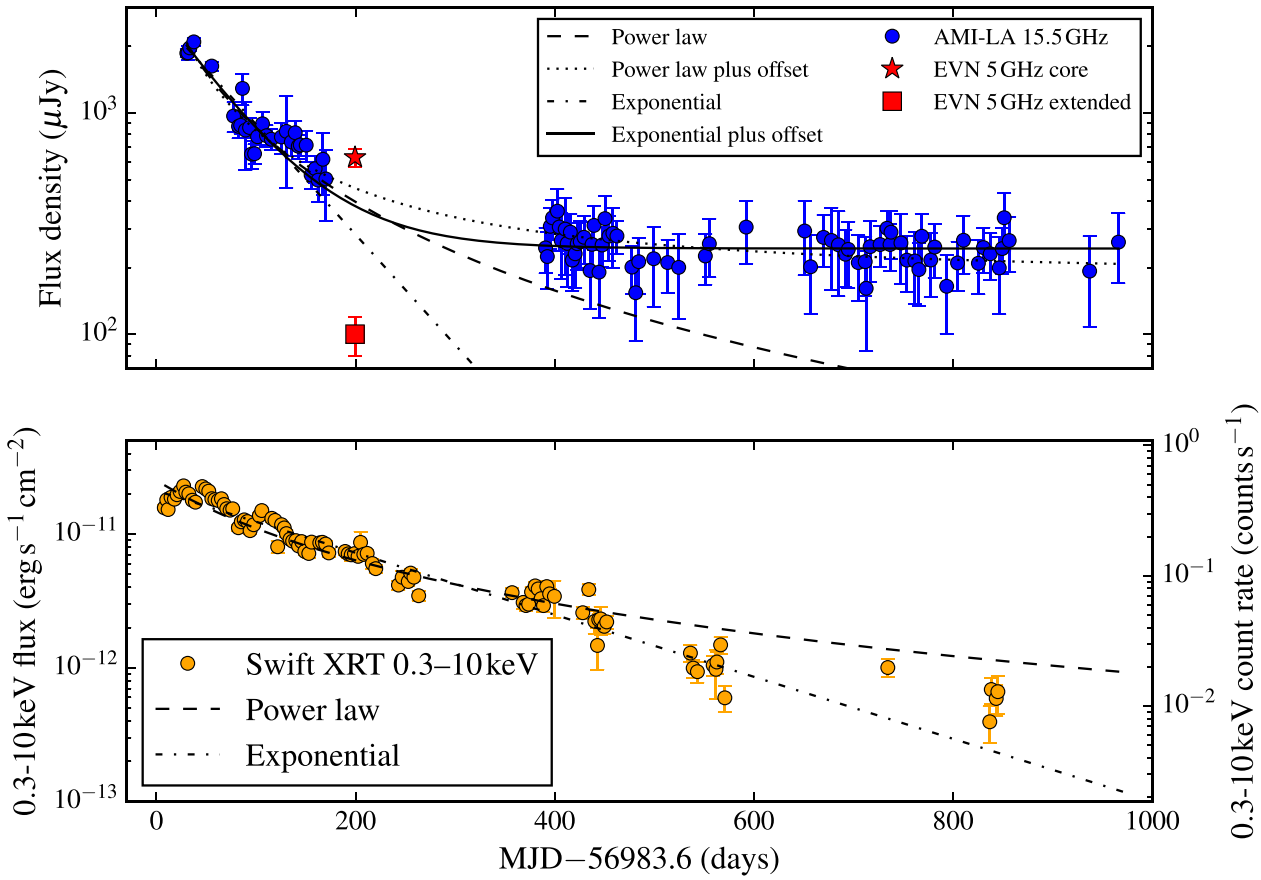

Figure 1. Radio and X-ray emission over the first 1000 d post-detection of TDE ASASSN-14li. Upper panel: blue circles indicate observed radio flux measured by the AMI-LA at 15.5 GHz (15.7 GHz for epochs up to MJD − 56983.6 = 200). Lower panel: *Swift* XRT observations in the 0.3–10 keV energy band, measured in both counts per second and flux. In both panels error bars indicate 1σ uncertainties on measurements, dashed lines show a power-law decay with the exponent fixed to $t^{-5/3}$, and dash–dotted lines show an exponential decay. Exponential and power-law decays plus a constant offset are fitted to the radio data only and are shown by solid and dotted lines, respectively. The red star and square indicate measurements of core and extended components (respectively) of ASASSN-14li at 5 GHz with the EVN (Romero-Cañizales et al. 2016). Fit parameters are summarized in Table 1. Note the logarithmic scale on the *y*-axis.

Pipeline (Swinbank et al. 2015). A detection threshold of 3.5-sigma was used for source identification, and a 3-sigma threshold was used for fitting the source in the image plane for each observation. A 2D Gaussian, with the same dimensions as the clean beam, was used to fit the unresolved source at phase centre (corresponding to ASASSN-14li). Typical dimensions of the clean beam major and minor axis FWHM are ∼60 and ∼30 arcsec, respectively. The AMI-LA light curve is shown in the top panel of Fig. 1. Stacking the plateau phase radio observations in each of eight equally spaced frequency bands, we are able to estimate a spectral index of -0.9 ± 0.5.

3 RESULTS

3.1 Characterizing the decays

Radio and X-ray light curves of ASASSN-14li for ∼1000 d post-discovery are shown in Fig. 1, along with power-law and exponential fits to both data sets. The fit parameters are summarized in Table 1. We find that the X-ray light curve is better characterized by an exponential decay, rather than the canonical (e.g. Phinney 1989) $-5/3$ exponent power-law decay, demonstrated by the significantly improved reduced chi-squared statistic (Table 1). The large reduced chi-squared values, however, indicate that while we may be describing the long-term trends in the light curve, there is significant deviation from this simple decay model on shorter time-scales. For ease of discussion we will refer to epochs up to MJD − 56983.6 = 200 as the decay phase (although it is only the radio light curve that ceases to decay after this date), and later observations as the plateau phase. When fitting the radio light curve, we opt to consider two cases. First, we fit the decay phase during the first ∼200 d and find that the $-5/3$ power law explains the data marginally better than an exponential. The whole set of radio observations (decay and plateau) is well characterized by an exponential decay plus a constant offset (a $-5/3$ power law plus offset provided a worse fit). Whilst it would be natural to attempt to fit the decays with a varying index and start date we are unable to resolve the inherent degeneracy in these two parameters given that we do not observe the peak of the light curve. Using the most recent date of non-detection of ASASSN-14li at optical wavelengths presented in Brown et al. (2017a) as an estimate of the start time allows for a crude estimate of the power-law index to be calculated. The index, when adopting this start date, is similar to $-5/3$ but the reduced chi-squared is still significantly worse than for an exponential decay.

Table 1. Summary of light-curve fitting parameters for the exponential, exponential plus offset, and power-law fits shown in Fig. 1. The (entire) radio light curve is best fitted by an exponential plus constant offset which is used to estimate the plateau flux. The reduced chi-squared statistic, $\chi^2_{\rm red}$, indicates that the X-ray light curve is significantly better fitted by an exponential rather than a $-5/3$ power law. The large $\chi^2_{\rm red}$ values result from deviations from simple decay models.

		Radio			
Fit type	t_0 (MJD $-$ $t_{\rm d}$)	Decay time-scale (d)	Power-law index	Offset (μJy)	$\chi^2_{\rm red}$
Exponential[a]	–	87 ± 6	–	–	3.24
Exponential and offset[b]	–	66 ± 3	–	244 ± 8	0.99
Power law[a,c]	-71 ± 8	–	$-5/3$	–	2.48
Power law and offset[b,c]	-47 ± 5	–	$-5/3$	180 ± 10	0.94
		X-ray			
Fit type	t_0 (MJD $-$ $t_{\rm d}$)	Decay time-scale (d)	Power-law index	–	$\chi^2_{\rm red}$
Exponential	–	187 ± 6	–	–	8.54
Power law[c]	-155 ± 9	–	$-5/3$	–	13.99
Power law[d]	-132.35	–	-1.60 ± 0.05	–	14.95

Notes. [a]Only radio measurements in decay phase used for fit.
[b]All radio measurements used for fit.
[c]Power-law index fixed to $-5/3$.
[d]Start date fixed.

3.2 Decay phase X-ray–radio correlation

In order to correlate the X-ray and radio observations of ASASSN-14li, which were not simultaneous, we binned each light curve into bins of width 4 d and compared the radio and X-ray flux where both had been measured in the same bin. This width was found to optimize the number of data points available for comparison. If multiple measurements at the same wavelength were contained within a specific bin then a numerical average of the data was used to represent the flux in that bin. In the case of either light curve having no data within a bin, no comparison was made. In order to ensure we were only comparing radio and X-ray emission resulting from the TDE, and not just from the host, we exclude data taken during the plateau phase from our correlation analysis. Before this date both the X-ray and radio emission were still declining and thus dominated by the TDE. We find that the radio flux density and X-ray flux (and thus the luminosities) are strongly correlated during the decay phase. The form of the relationship is $L_{\rm R} \propto L_{\rm X}^{1.9\pm0.2}$ and the Spearman rank correlation coefficient is 0.86. To obtain these results we subtract the plateau radio measurement of 244 ± 8 μJy from the decay phase radio observations. $L_{\rm R}$ is the isotropic, monochromatic, luminosity at 15.7 GHz and $L_{\rm X}$ is the X-ray luminosity in the 0.3–10 keV energy band. The correlation can be seen in Fig. 2.

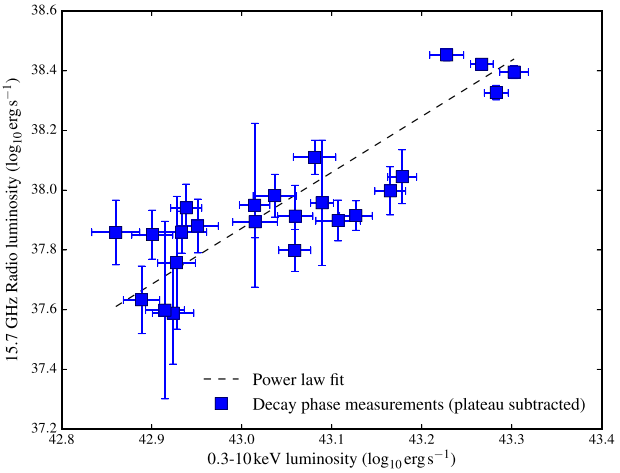

Figure 2. Radio–X-ray correlation for ASASSN-14li, produced by binning the respective light curves during the decay phase and subtracting the plateau flux of 244 μJy. The black dotted line is a fit to the data, with a best-fitting power-law index of $\alpha = 1.9 \pm 0.2$ ($L_{\rm R} \propto L_{\rm X}^{\alpha}$).

4 DISCUSSION

4.1 Explaining the radio plateau

It is clear from Fig. 1 that the radio light curve plateaus from an initial fading phase into a phase of constant flux of around 250 μJy which it has maintained for around 600 d. During the radio plateau period, the X-ray count rate continues to decline, showing no sign of mirroring the behaviour at 15.5 GHz. We discuss a number of possible contributors to the radio flux density plateau observed by the AMI-LA.

4.1.1 Host galaxy radio emission

We assume here that the plateau emission is unconnected to the TDE, which presumably continues to decline, and discuss briefly below its possible origin. The host galaxy of ASASSN-14li, PGC 043234, has archival measurements in the FIRST (November 1999) and NVSS (December 1993) surveys, both at 1.4 GHz (Becker, White & Helfand 1995; Condon et al. 1998). The measured flux densities are 2.96 ± 0.15 and 3.2 ± 0.4 mJy, respectively. Due to the resolution of the AMI-LA we are unable to resolve individual sources in the host galaxy and so all radio emitting elements from the galaxy will be observed to be combined into a single unresolved source.

First, supernova remnants (SNR) in the host galaxy could be responsible for background emission. The small-scale radio morphology of PGC 043234 has not been probed with long baseline observations (outside of the central few parsecs; Romero-Cañizales et al. 2016) so we must turn to analogous galaxies which have been studied more extensively. Arp220 is a nearby (77 Mpc) ultra-luminous infrared galaxy, which has been well studied at 18, 13, 6, 3.6 (Smith et al. 1998; Parra et al. 2007) and most usefully 2 cm (15 GHz) with very long baseline interferometry (VLBI; Batejat et al. 2011). These observations revealed a population of compact (sub-parsec) sources which are believed to be a mixture of

supernovae (SNe) and SNR. The 15 GHz radio flux from these individual sources ranges from 91 to 693 μJy which would correspond to 66 and 504 μJy at the distance of ASASSN-14li. Although this galaxy is a more extreme environment than the host of ASASSN-14li, it illustrates that even a single radio loud SNe or SNR, or a population of fainter objects, could be responsible for the observed radio plateau of ASASSN-14li.

An alternative, and more likely, possibility is emission from relic radio lobes from past AGN activity (discussed briefly also in van Velzen et al. 2016). Such lobes would be expected to remain constant in flux over long time-scales and to have an optically thin spectrum. Considering the lack of star formation indicators (discussed in Prieto et al. 2016; Alexander et al. 2016; van Velzen et al. 2016) in PGC 043234, the clear presence of a SMBH (hence the TDE) and the EVN observations revealing the majority of the flux to be combined within a few parsecs of the central object, we conclude that past AGN activity is the more likely scenario for the quiescent component.

Optically thin relic AGN lobes with a spectral index of approximately −0.9 (consistent with both our in-band measurements and those reported towards the end of the decay phase by Alexander et al. 2016) and a 15.5 GHz flux density of 244 μJy would correspond to a 1.4 GHz flux density of ∼2.1 mJy, broadly consistent the quiescent component assumed in Alexander et al. (2016). It has been proposed (van Velzen et al. 2016) that the onset of the TDE suppressed optically thick emission from a steady AGN jet in PGC 043234. Our discovery of a plateau is not inconsistent with this idea, if the system contained both AGN lobes and a compact jet pre-TDE (the sum of which gave the archival 1.4 GHz measurements of ∼3 mJy). It is also possible (Alexander et al. 2016) that the observed decline in 1.4 GHz emission in the 16 years since the FIRST measurement is simply due to long-term AGN variability of a compact component.

4.1.2 Radio emission still from ASASSN-14li

We also consider the possibility that the radio emission we are observing is now steady emission from the TDE. It is, however, hard to reconcile the combined observed X-ray and radio behaviour with any of the TDE models currently being considered. If the radio emission results from some form of outflow (radiatively driven wind, unbound material, discrete jet launch) we can see no reason why the radio emission would stop declining, despite it not being coupled to the likely source of X-ray emission (the accretion disc). In the case of core-jet activity we would expect the X-ray and radio emission to remain coupled. In all scenarios, barring an unexpected increase in accretion rate, the decaying nature of the X-ray light curve is expected. Given the numerous possibilities for constant (on the time-scale of the decay of ASASSN-14li) sources of radio emission in PGC 043234 (as discussed in Section 4.1.1) and the fact that we can see no physical motivation for the radio emission in any of the currently considered models (core-jet emission, relativistic jet, radiatively driven wind, shocking disrupted material) to plateau, we strongly disfavour this scenario, instead attributing the quiescent radio flux density to background emission from PGC 043234.

4.2 X-ray–radio correlation

It is clear that prior to the radio plateau the radio and X-ray emission are fading together (Fig. 1). When correlating the decay phase data we subtract the plateau emission and find a strong positive correlation between the X-ray and radio flux (Fig. 2). The correlation can be described by a power law, with a power-law index of $\alpha = 1.9 \pm 0.2$ ($L_{\rm R} \propto L_{\rm X}^{\alpha}$). This correlation can be interpreted in two ways.

The more conventional explanation is that the core X-ray emission arises in the accretion flow while the radio emission is from decoupled ejecta, and both are fading independently. Two variants of this scenario are outlined in Krolik et al. (2016) and Alexander et al. (2016). Even under the assumption that one of these models is correct, it is not clear if or how our new radio and X-ray data could discriminate between them.

Alternatively, the core X-ray and radio emission may be correlated because they are coupled via an accretion flow feeding a core jet. Such an interpretation is not generally invoked for TDEs, although for this source it is also raised to explain shorter-time radio and X-ray correlations (Pasham & van Velzen 2017). The observed correlation, $L_{\rm R} \propto L_{\rm X}^{1.9\pm0.2}$, is similar to that observed for stellar mass black holes in 'radio quiet' black hole X-ray binaries (e.g. Coriat et al. 2011). While in such systems the radio spectrum is usually flatter than is observed in ASASSN-14li (Alexander et al. 2016 and this work), it is not inconsistent with the range observed (Espinasse & Fender 2017). Typically core-jet emission in stellar mass black hole binaries is seen to coincide with a hard X-ray spectrum, peaking at ∼100 keV. The majority of X-ray photons from ASASSN-14li are below ∼1 keV; however not enough is known about the nature of the accretion flows in TDEs for this to exclude core-jet emission. We also note that there are examples of galactic X-ray binaries (e.g. GRS 1915+105; Fender & Belloni 2004) showing core radio emission with a soft X-ray spectrum, when averaged over a certain time period and at a high accretion rate.

Applying the approximate relationship between core radio luminosity and jet kinetic power presented in Merloni & Heinz (2007) to the peak radio luminosity of ASASSN-14li gives $L_{\rm jet} \sim 10^{43}$ erg s^{-1}. It is reassuring to note that Pasham & van Velzen (2017) find that ASASSN-14li falls on the Fundamental Plane of black hole activity (Merloni, Heinz & di Matteo 2003), although with the caveat that the X-ray luminosity was derived using the 0.3–1 keV energy band rather than the traditional 2–10 keV. Further VLBI observations along the lines of those reported in Romero-Cañizales et al. (2016) may help to resolve uncertainties in the origin of the radio emission.

4.3 Light-curve fits

It is clear that the forced $t^{-5/3}$ power-law fit does not well describe the X-ray data compared to the exponential decay, demonstrated by the significantly increased reduced chi-squared statistic and the overestimate of the late time flux. It is, however, likely that the fit would be significantly improved if there was a better constraint on the start date (t_0) of the flare (see more estimates in Brown et al. 2017a). In either case it is evident that a simple decay model for the X-ray emission from ASASSN-14li is not explaining the significant short-term variability in the light curve, demonstrated by the large reduced chi-square value. During the first ∼150 d of X-ray observations, deviations from the simple decay models are dominated by an apparently quasi-periodic signal. We do not speculate on the physical origin of this borderline significant feature, but plan to present analysis in a future work.

The early time radio light curve is well characterized by both a −5/3 power law and an exponential (although marginally better by a power law), and the entire data set is well fitted by an exponential plus constant offset. The exponential fits for the light curves provide characteristic decay times for the X-ray and radio emission which are ∼190 and ∼90 d, respectively. Fitting the radio light curve with a free index suffers from the same issues as the X-ray light curve;

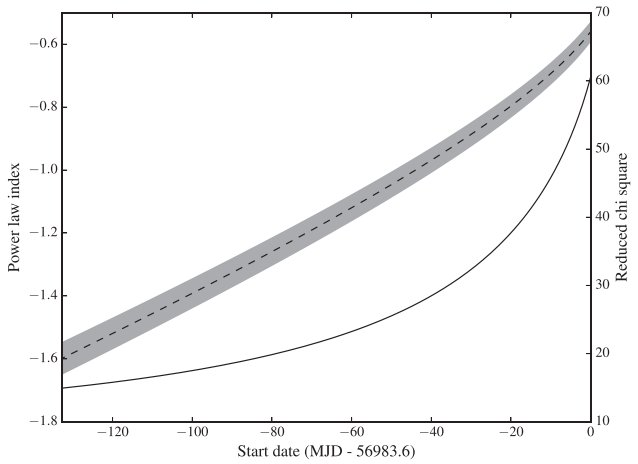

Figure 3. Best-fitting power-law index for the X-ray light curve (black dashed line and shaded 1-sigma confidence region), and the associated reduced chi-square (solid black line) as a function of fixed start date (t_0).

however see Auchettl, Guillochon & Ramirez-Ruiz (2017) for a more detailed analysis of TDE decays at X-ray wavelengths.

If core–jet coupling is present in ASASSN-14li we might expect short-term variation in the X-ray light curve to be mirrored in the radio light curve, a possibility explored in Pasham & van Velzen (2017). The observation that the short-term radio variability appears to be less pronounced than in the X-ray light curve could be explained by the fact that the radio emitting region is both larger than, and removed from, the X-ray emitting region, which would result in short-term variability being washed out.

The assumed start date of X-ray emission (t_0 in Table 1) has a significant impact on the power-law index derived to describe the decay. It is important to constrain this parameter as well as possible, as the decay index provides important information on e.g. the mass return and accretion rate and potentially the make-up of the disrupted body (e.g. Lodato, King & Pringle 2009; Guillochon & Ramirez-Ruiz 2015; Bonnerot et al. 2016). It may also be the case that these decays are not power laws at all. To investigate this effect, we fit a power-law decay to the X-ray light curve with a varying t_0, beginning from the latest ASASSN non-detection ($t_0 = -132.35$; Brown et al. 2017a; although note that this is an optical, not X-ray, non-detection) and ending at the ASASSN discovery date ($t_0 = 0$) which is shown in Fig. 3. For the range of start dates considered the best-fitting power-law index varies between ~ -1.6 and ~ -0.6 with the goodness of fit reducing dramatically with later start dates. Care must be taken, however, as earlier start dates will naturally provide a better fit and so without prompt observations that sample the rise and peak of the light curve the true start date and power-law index cannot be well constrained. For example, Auchettl et al. (2017) find a best-fitting power-law index of -0.92 ± 0.12 (although they bin the X-ray light curve with much larger bins) whereas van Velzen et al. (2016) report an index of -1.7.

5 CONCLUSIONS

We present radio observations of the TDE ASASSN-14li from the Arcminute Microkelvin Imager Large Array and explore their relation to new and archival *Swift* X-ray observations of the source. We find that the evolution at both wavelengths is well described by an exponential decay. We then show that the early time ($\sim$200 d) X-ray and radio emission are correlated, with a power-law index of $\alpha = 1.9 \pm 0.2$, with $L_R \propto L_X^{\alpha}$. This correlation suggests the possibility that we are observing core disc–jet coupling from ASASSN-14li, which would contradict previous interpretations of the site of radio emission. While the X-ray emission from the source decays in a similar way throughout the observing campaign, the radio emission tails off into a plateau at $\sim$250 μJy. We discuss the possibility that this radio plateau is constant emission from the TDE, but conclude that it is most likely that we are now observing background radio emission from ASASSN-14li's host galaxy, which we show could easily arise from SNRs or low level AGN activity (although we favour archival AGN activity). If the radio emission from ASASSN-14li has continued to follow the correlation derived from the first $\sim$200 d of observations, using the most recent X-ray measurements we would expect a radio flux from the TDE of $\sim$5 μJy. We therefore expect that, barring a re-flaring event, radio observations of ASASSN-14li with the AMI-LA will remain at their current level. Future X-ray and radio observations will allow us to confirm or refute our interpretation.

ACKNOWLEDGEMENTS

We would like to thank the staff at the Mullard Radio Astronomy Observatory for scheduling and carrying out the AMI-LA observations. This work made use of data supplied by the UK Swift Science Data Centre at the University of Leicester. JSB would like to acknowledge the support given by the Science and Technologies Facilities Council (STFC) through an STFC studentship. YCP is supported by a Trinity College JRF. The AMI telescope is supported by the European Research Council under grant ERC-2012-StG-307215 LODESTONE, the UK Science and Technology Facilities Council (STFC), and the University of Cambridge. We thank the anonymous referee for their helpful comments.

REFERENCES

Alexander K. D., Berger E., Guillochon J., Zauderer B. A., Williams P. K. G., 2016, ApJ, 819, L25
Alexander K. D., Wieringa M. H., Berger E., Saxton R. D., Komossa S., 2017, ApJ, 837, 153
Arcavi I. et al., 2014, ApJ, 793, 38
Auchettl K., Guillochon J., Ramirez-Ruiz E., 2017, ApJ, 838, 149
Batejat F., Conway J. E., Hurley R., Parra R., Diamond P. J., Lonsdale C. J., Lonsdale C. J., 2011, ApJ, 740, 95
Becker R. H., White R. L., Helfand D. J., 1995, ApJ, 450, 559
Bonnerot C., Rossi E. M., Lodato G., Price D. J., 2016, MNRAS, 455, 2253
Brown J. S., Holoien T. W.-S., Auchettl K., Stanek K. Z., Kochanek C. S., Shappee B. J., Prieto J. L., Grupe D., 2017a, MNRAS, 466, 4904
Brown G. C. et al., 2017b, MNRAS, 472, 4469
Burrows D. N. et al., 2011, Nature, 476, 421
Cenko S. B. et al., 2012, ApJ, 753, 77
Condon J. J., Cotton W. D., Greisen E. W., Yin Q. F., Perley R. A., Taylor G. B., Broderick J. J., 1998, AJ, 115, 1693
Coriat M. et al., 2011, MNRAS, 414, 677
Davies M. L. et al., 2009, MNRAS, 400, 984
Esquej P., Saxton R. D., Freyberg M. J., Read A. M., Altieri B., Sanchez-Portal M., Hasinger G., 2007, A&A, 462, L49
Evans C. R., Kochanek C. S., 1989, ApJ, 346, L13
Evans P. A. et al., 2007, A&A, 469, 379
Evans P. A. et al., 2009, MNRAS, 397, 1177
Fender R., Belloni T., 2004, ARA&A, 42, 317
Gehrels N. et al., 2004, ApJ, 611, 1005
Gezari S. et al., 2009, ApJ, 698, 1367
Goad M. R. et al., 2007, A&A, 476, 1401
Guillochon J., Ramirez-Ruiz E., 2015, ApJ, 809, 166
Guillochon J., Manukian H., Ramirez-Ruiz E., 2014, ApJ, 783, 23
Hayasaki K., Stone N., Loeb A., 2013, MNRAS, 434, 909
Hickish J. et al., 2018, , MNRAS, in press
Holoien T. W.-S. et al., 2016, MNRAS, 455, 2918

Irwin J. A., Henriksen R. N., Krause M., Wang Q. D., Wiegert T., Murphy E. J., Heald G., Perlman E., 2015, ApJ, 809, 172
Jose J. et al., 2014, Astron. Telegram, 6777
Komossa S., Bade N., 1999, A&A, 343, 775
Krolik J., Piran T., Svirski G., Cheng R. M., 2016, ApJ, 827, 127
Lodato G., King A. R., Pringle J. E., 2009, MNRAS, 392, 332
McMullin J. P., Waters B., Schiebel D., Young W., Golap K., 2007, in Shaw R. A., Hill F., Bell D. J., eds, ASP Conf. Ser. Vol. 376, Astronomical Data Analysis Software and Systems XVI. Astron. Soc. Pac., San Francisco, p. 127
Merloni A., Heinz S., 2007, MNRAS, 381, 589
Merloni A., Heinz S., di Matteo T., 2003, MNRAS, 345, 1057
Miller J. M. et al., 2015, Nature, 526, 542
Parra R., Conway J. E., Diamond P. J., Thrall H., Lonsdale C. J., Lonsdale C. J., Smith H. E., 2007, ApJ, 659, 314
Pasham D. R., van Velzen S., 2017, ApJ, preprint (arXiv:1709.02882)
Pasham D. R., Cenko S. B., Sadowski A., Guillochon J., Stone N. C., van Velzen S., Cannizzo J. K., 2017, ApJ, 837, L30
Phinney E. S., 1989, in Morris M., ed., IAU Symp. Vol. 136. The Center of the Galaxy. Kluwer Academic Publishers, Dordrecht, p. 543
Piran T., Svirski G., Krolik J., Cheng R. M., Shiokawa H., 2015, ApJ, 806, 164
Prieto J. L. et al., 2016, ApJ, 830, L32
Rees M. J., 1988, Nature, 333, 523
Romero-Cañizales C., Prieto J. L., Chen X., Kochanek C. S., Dong S., Holoien T. W.-S., Stanek K. Z., Liu F., 2016, ApJ, 832, L10
Shappee B. J. et al., 2014, ApJ, 788, 48
Smith H. E., Lonsdale C. J., Lonsdale C. J., Diamond P. J., 1998, ApJ, 493, L17
Swinbank J. D. et al., 2015, Astron. Comput., 11, 25
van Velzen S. et al., 2011, ApJ, 741, 73
van Velzen S. et al., 2016, Science, 351, 62
Voges W. et al., 1999, A&A, 349, 389
Zauderer B. A. et al., 2011, Nature, 476, 425
Zwart J. T. L. et al., 2008, MNRAS, 391, 1545

APPENDIX: OBSERVATIONS

A1 Radio observations

Table A1. AMI-LA radio observations of ASASSN-14li.

Date (MJD)	Frequency (GHz)	Flux density (μJy)	Flux density error (μJy)
57014.078	15.7	1865	83
57015.170	15.7	1871	141
57017.096	15.7	1969	67
57021.111	15.7	2096	84
57039.088	15.7	1629	78
57061.053	15.7	969	150
57065.995	15.7	870	103
57068.089	15.7	879	72
57069.970	15.7	1291	209
57072.982	15.7	836	286
57077.055	15.7	860	86
57079.057	15.7	652	93
57082.105	15.7	654	66
57085.088	15.7	781	61
57090.081	15.7	894	121
57094.062	15.7	789	90
57098.952	15.7	761	82
57109.041	15.7	779	127
57113.984	15.7	826	367
57118.978	15.7	740	103
57122.941	15.7	814	104

Table A1 – *continued*

Date (MJD)	Frequency (GHz)	Flux density (μJy)	Flux density error (μJy)
57125.982	15.7	708	87
57127.975	15.7	717	76
57133.958	15.7	715	117
57138.941	15.7	525	73
57142.951	15.7	560	79
57145.921	15.7	497	99
57150.749	15.7	617	191
57153.735	15.7	503	177
57374.323	15.5	245	57
57376.128	15.5	224	65
57379.112	15.5	307	65
57381.291	15.5	336	70
57386.186	15.5	360	93
57388.098	15.5	305	68
57390.092	15.5	265	88
57392.087	15.5	132	89
57394.081	15.5	298	114
57396.066	15.5	257	93
57399.243	15.5	289	60
57401.211	15.5	216	59
57404.097	15.5	231	69
57406.156	15.5	257	61
57409.182	15.5	262	63
57413.019	15.5	274	68
57419.077	15.5	194	63
57421.028	15.5	255	66
57422.981	15.5	310	71
57428.013	15.5	191	72
57431.133	15.5	253	51
57434.038	15.5	333	87
57438.027	15.5	278	63
57441.950	15.5	286	87
57446.040	15.5	278	46
57461.083	15.5	201	49
57464.874	15.5	154	61
57467.897	15.5	213	60
57482.937	15.5	219	86
57496.982	15.5	211	57
57500.989	15.5	169	72
57508.040	15.5	200	83
57534.795	15.5	226	58
57538.815	15.5	256	76
57575.815	15.5	305	96
57632.565	15.5	143	99
57634.542	15.5	293	108
57640.501	15.5	202	78
57649.483	15.5	187	89
57653.480	15.5	274	72
57661.399	15.5	265	108
57668.399	15.5	254	105
57675.482	15.5	230	67
57678.358	15.5	242	81
57688.384	15.5	211	69
57695.340	15.5	213	64
57696.316	15.5	161	78
57700.305	15.5	249	77
57710.302	15.5	254	53
57717.262	15.5	301	58
57720.272	15.5	254	61
57721.227	15.5	289	70
57731.224	15.5	258	90
57737.204	15.5	216	61
57745.226	15.5	214	77
57749.236	15.5	196	62

Table A1 – *continued*

Date (MJD)	Frequency (GHz)	Flux density (μJy)	Flux density error (μJy)
57752.184	15.5	277	74
57761.183	15.5	216	70
57765.172	15.5	248	68
57769.141	15.5	199	95
57777.143	15.5	165	64
57783.100	15.5	195	130
57788.087	15.5	210	52
57794.050	15.5	266	78
57799.122	15.5	218	89
57809.033	15.5	209	58
57814.037	15.5	246	57
57820.918	15.5	231	54
57829.971	15.5	199	77
57832.963	15.5	244	57
57834.958	15.5	336	98
57839.945	15.5	265	74
57888.911	15.5	188	119
57920.723	15.5	193	85
57949.661	15.5	261	91

A2 X-ray observations

Table A2. *Swift* 0.3–10 keV observations of ASASSN-14li.

Date (MJD)	Count rate (counts s^{-1})	Count rate error (counts s^{-1})	Flux (10^{12} erg s^{-1} cm^{-2})	Flux error (10^{12} erg s^{-1} cm^{-2})
56998.259	0.410	0.016	18.8	0.7
57001.637	0.397	0.017	18.2	0.8
57004.197	0.429	0.024	19.7	1.0
57007.296	0.454	0.017	20.8	0.8
57010.835	0.524	0.018	24.0	0.8
57013.099	0.448	0.016	20.6	0.7
57016.092	0.435	0.019	20.0	0.9
57019.576	0.390	0.015	17.9	0.7
57022.745	0.377	0.016	17.3	0.7
57029.582	0.494	0.015	22.7	0.7
57033.144	0.474	0.023	21.7	1.0
57036.110	0.456	0.021	20.9	1.0
57039.234	0.401	0.016	18.4	0.7
57042.296	0.394	0.018	18.1	0.8
57045.624	0.388	0.015	17.8	0.7
57048.821	0.400	0.016	18.4	0.7
57051.534	0.363	0.017	16.7	0.8
57054.139	0.337	0.012	15.5	0.6
57057.560	0.329	0.013	15.1	0.6
57060.165	0.337	0.012	15.5	0.6
57065.849	0.243	0.014	11.2	0.6
57068.779	0.269	0.015	12.3	0.7
57071.737	0.278	0.012	12.8	0.6
57074.910	0.270	0.011	12.4	0.5
57077.633	0.231	0.013	10.6	0.6
57081.189	0.256	0.010	11.8	0.5
57086.917	0.299	0.013	13.7	0.6
57089.381	0.327	0.013	15.0	0.6
57099.421	0.286	0.016	13.1	0.7
57102.655	0.276	0.012	12.7	0.6
57105.311	0.175	0.019	8.0	0.9
57109.208	0.256	0.012	11.8	0.6
57111.933	0.242	0.012	11.1	0.6
57114.128	0.220	0.014	10.1	0.6
57117.720	0.199	0.011	9.1	0.5

Table A2 – *continued*

Date (MJD)	Count rate (counts s^{-1})	Count rate error (counts s^{-1})	Flux (10^{12} erg s^{-1} cm^{-2})	Flux error (10^{12} erg s^{-1} cm^{-2})
57120.317	0.193	0.011	8.9	0.5
57123.578	0.195	0.010	9.0	0.5
57126.243	0.178	0.009	8.2	0.4
57129.400	0.191	0.012	8.8	0.6
57132.560	0.162	0.010	7.4	0.5
57136.560	0.156	0.012	7.2	0.6
57139.347	0.190	0.011	8.7	0.5
57147.597	0.187	0.010	8.6	0.5
57150.256	0.189	0.009	8.7	0.4
57153.486	0.183	0.009	8.4	0.4
57156.647	0.157	0.010	7.2	0.5
57173.106	0.161	0.010	7.4	0.5
57176.134	0.155	0.010	7.1	0.5
57179.194	0.152	0.016	7.0	0.7
57182.465	0.155	0.013	7.1	0.6
57186.055	0.148	0.010	6.8	0.5
57188.549	0.189	0.039	8.7	2.0
57191.845	0.154	0.009	7.1	0.4
57195.195	0.156	0.009	7.2	0.4
57200.382	0.131	0.011	6.0	0.5
57203.807	0.120	0.009	5.5	0.4
57226.617	0.090	0.007	4.1	0.3
57230.379	0.103	0.011	4.7	0.5
57236.470	0.096	0.007	4.4	0.3
57238.860	0.111	0.008	5.1	0.4
57242.120	0.104	0.007	4.8	0.3
57246.907	0.075	0.006	3.5	0.3
57340.745	0.079	0.006	3.6	0.3
57351.843	0.067	0.007	3.1	0.3
57354.698	0.063	0.006	2.9	0.3
57357.365	0.065	0.006	3.0	0.3
57360.258	0.080	0.007	3.7	0.3
57363.951	0.089	0.006	4.1	0.3
57366.940	0.084	0.006	3.9	0.3
57369.900	0.071	0.006	3.3	0.3
57372.255	0.063	0.007	2.9	0.3
57375.579	0.088	0.009	4.0	0.4
57378.411	0.078	0.007	3.6	0.3
57383.203	0.074	0.023	3.4	1.0
57411.684	0.056	0.006	2.6	0.3
57417.730	0.084	0.008	3.9	0.4
57423.806	0.048	0.009	2.2	0.4
57426.466	0.032	0.011	1.5	0.5
57427.758	0.050	0.006	2.3	0.3
57429.669	0.050	0.012	2.3	0.6
57433.319	0.044	0.006	2.0	0.3
57435.743	0.048	0.005	2.2	0.2
57519.819	0.028	0.004	1.3	0.2
57522.607	0.021	0.003	1.0	0.1
57526.827	0.020	0.004	0.9	0.2
57542.686	0.022	0.004	1.0	0.2
57545.455	0.021	0.009	1.0	0.4
57546.401	0.024	0.005	1.1	0.2
57550.131	0.032	0.005	1.5	0.2
57554.383	0.013	0.003	0.6	0.1
57718.041	0.022	0.003	1.0	0.1
57820.434	0.008	0.003	0.4	0.1
57821.966	0.015	0.003	0.7	0.1
57826.917	0.013	0.003	0.6	0.1
57828.568	0.014	0.005	0.7	0.2

This paper has been typeset from a TEX/LATEX file prepared by the author.